Geophysical Research Letters

RESEARCH LETTER
10.1029/2024GL112411

# Predictable Patterns of Seasonal Atmospheric River Variability Over North America During Winter

**Joseph P. Clark**[1], **Nathaniel C. Johnson**[2], **Mingyu Park**[1], **Miguel Bernardez**[2,3], and **Thomas L. Delworth**[2]

[1]Program in Atmospheric and Oceanic Sciences, Princeton University, Princeton, NJ, USA, [2]National Oceanic and Atmospheric Administration/Geophysical Fluid Dynamics Laboratory, Princeton, NJ, USA, [3]University Corporation for Atmospheric Research, Boulder, CO, USA

**Key Points:**

- Three physically interpretable modes explain the skill of winter atmospheric river (AR) frequency and precipitation predictions
- The modes include the AR response to El Niño-Southern Oscillation, global warming, and convection over the western equatorial Pacific
- Together these three modes explain about 19% of the total winter AR variance over the Pacific-North America domain

**Supporting Information:**

Supporting Information may be found in the online version of this article.

**Correspondence to:**

J. P. Clark,
jc7377@princeton.edu

**Citation:**

Clark, J. P., Johnson, N. C., Park, M., Bernardez, M., & Delworth, T. L. (2025). Predictable patterns of seasonal atmospheric river variability over North America during winter. *Geophysical Research Letters*, *52*, e2024GL112411. https://doi.org/10.1029/2024GL112411

Received 12 SEP 2024
Accepted 7 MAR 2025

**Author Contributions:**

**Conceptualization:** Joseph P. Clark, Nathaniel C. Johnson, Miguel Bernardez
**Formal analysis:** Joseph P. Clark
**Funding acquisition:** Nathaniel C. Johnson, Thomas L. Delworth
**Investigation:** Joseph P. Clark
**Methodology:** Joseph P. Clark, Nathaniel C. Johnson
**Project administration:** Thomas L. Delworth
**Software:** Joseph P. Clark
**Supervision:** Nathaniel C. Johnson
**Visualization:** Joseph P. Clark
**Writing – original draft:** Joseph P. Clark
**Writing – review & editing:** Nathaniel C. Johnson, Miguel Bernardez, Thomas L. Delworth



**Abstract** Atmospheric rivers (ARs) are elongated areas of pronounced atmospheric water vapor transport that play an important role in the hydrological cycle over North America during winter. We investigate the sources of winter seasonal AR predictability over North America using average predictability time (APT) analysis. The skill of seasonal AR frequency predictions, in dynamical model forecasts provided by the Seamless System for Prediction and Earth System Research, is nearly entirely attributable to three physically interpretable APT modes that together represent about 19% of the total seasonal AR frequency variance. These three modes represent the AR response to the El Niño-Southern Oscillation, anthropogenic forcing and equatorial heating over the eastern flank of the western Pacific warm pool, respectively. We further show that these three modes, calculated from AR frequency, explain nearly all winter seasonal precipitation forecast skill over North America.

**Plain Language Summary** Atmospheric rivers (ARs) are long and narrow atmospheric weather systems that carry large amounts of water vapor. ARs typically cover areas larger than 300,000 km$^2$ and accompany significant precipitation changes over the U.S. Previous research has shown that we can predict, with modest accuracy, how often ARs will occur in upcoming winter seasons over the U.S. In this study, we investigate what factors contributed to these predictions of wintertime AR frequency. We use a method called average predictability time analysis to identify predictable AR patterns over North America from a model seasonal forecast data set. Three key weather patterns are identified, which are closely tied to (a) El Niño Southern Oscillation, (b) anthropogenic climate change, and (c) an equatorial sea surface temperature anomaly west of the dateline. In our current modeling systems, the overall accuracy of our AR predictions is owed nearly entirely to these three weather patterns.

## 1. Introduction

Atmospheric rivers (ARs) are narrow and elongated areas of pronounced water vapor transport in the atmosphere that typically reside ahead of cold fronts within the warm conveyor belt of extratropical cyclones (Dettinger et al., 2015; Z. Zhang et al., 2019; Zhu & Newell, 1998). Collectively accounting for about 90% of the water vapor transport over midlatitudes (Zhu & Newell, 1998), ARs play an important role in extratropical climate. The hazardous conditions associated with ARs, including heavy precipitation and floods (e.g., Corringham et al., 2019; Ralph et al., 2006), pose significant challenges to society. However, ARs also represent a critical component to the hydrological cycle through, for example, their role in maintaining water availability and modulating snowpack (e.g., Dettinger, 2011, 2013; Guan et al., 2010). Both the detrimental and beneficial impacts associated with ARs underscore the need to improve AR prediction across a range of timescales.

Many studies have focused on AR predictability from synoptic to seasonal timescales, particularly along the U.S. west coast (e.g., Baggett et al., 2017; DeFlorio et al., 2018; DeFlorio, Waliser, Guan, et al., 2019; DeFlorio, Waliser, Ralph, et al., 2019; Nardi et al., 2018; Tseng et al., 2021; Wick et al., 2013; Zhou & Kim, 2018). On synoptic, that is, weather timescales (~10 days or less), daily AR prediction aligns well with conventional wisdom, with skill declining considerably for leads of greater than 7 days (DeFlorio et al., 2018; Nardi et al., 2018; Wick et al., 2013), though with extension possible if the state of El Niño-Southern Oscillation (ENSO) and the Pacific-North American teleconnections are considered (DeFlorio et al., 2018; Dong et al., 2024). AR prediction beyond the weather timescale, such as on subseasonal-to-seasonal timescales (i.e., about 2 weeks–3 months) tends to be less skillful (e.g., DeFlorio et al., 2018; DeFlorio, Waliser, Guan, et al., 2019; DeFlorio,

Waliser, Ralph, et al., 2019; W. Zhang et al., 2024), but some studies have nevertheless shown that skillful weekly averaged AR anomaly predictions are attainable, with skill over the U.S. west coast deriving mostly from large-scale teleconnections including those of the Madden-Julian Oscillation and the Quasi-Biennial Oscillation (QBO, Baggett et al., 2017; DeFlorio, Waliser, Ralph, et al., 2019; Mundhenk et al., 2018; Nardi et al., 2018). Globally, AR predictability on subseasonal timescales is also correlated to the Northern Annular Mode and ENSO (DeFlorio, Waliser, Guan, et al., 2019).

Although the skill and sources of subseasonal AR prediction are relatively well established, the skill and sources of seasonal AR prediction remain a subject of continuing investigation. Whereas Zhou and Kim (2018) found modest 3-month lead skill in predicting winter AR frequency using seasonal forecasts from the North American Multi-Model Ensemble (NMME, Kirtman et al., 2014), Tseng et al. (2021) showed that winter AR frequency can be skillfully forecast over much of the midlatitudes, particularly along the west coast of North America for lead times of up to 9 months using the Seamless System for Prediction and Earth System Research (SPEAR, Delworth et al., 2020), one of the models currently contributing to the NMME. Both Zhou and Kim (2018) and Tseng et al. (2021) presented evidence that ENSO plays a role in generating seasonal AR predictability. Zhou and Kim (2018) showed that seasonal AR forecasts over the U.S. west coast from the NMME are more skillful during ENSO years while Tseng et al. (2021) showed that the leading mode of seasonal AR variability over the North Pacific is correlated to ENSO in reanalysis data.

While it appears clear that ENSO plays a role in modulating seasonal AR predictability, it remains unclear whether additional predictability sources can contribute to skillful seasonal forecasts of AR activity and their associated precipitation over North America. This problem has received a heightened focus over the past decade, given the observed deviations from the expected ENSO precipitation response over the western U.S. during some recent ENSO events (DeFlorio et al., 2024; Jiang et al., 2022; Kumar & Chen, 2020). A significant fraction of AR activity over North America is owed to sources independent to ENSO (Ding & Wang, 2024). However, the ENSO-independent component to seasonal precipitation variability over California is not skillfully predicted in the NMME (Jiang et al., 2022). This limits precipitation prediction skill from dynamical models, as measured by the anomaly correlation, to values of near 0.3 over the U.S. west coast on seasonal timescales (as has been documented before, e.g., Kumar & Chen, 2020). Given this finding and that ARs drive a significant fraction of seasonal precipitation anomalies over western North America (Dettinger et al., 2011; Guan et al., 2010), it may be challenging to produce skillful seasonal AR and precipitation forecasts that outperform composites or linear regressions derived from statistical relationships with ENSO.

This gap in understanding, coupled with the profound impacts that ARs and their associated precipitation have on North America, motivates the following questions: (a) what are the sources of seasonal wintertime AR predictability over North America? (b) Is there any leverageable predictability source beyond canonical ENSO? (c) How much of the seasonal wintertime precipitation prediction skill can be explained by wintertime AR prediction skill?

To address these questions, we analyze data provided by the SPEAR prediction system. In Section 2 we discuss the data and methods used, including the hindcast and real-time forecast simulations provided by the SPEAR prediction system. Section 3 discusses the results, which covers the sources of seasonal AR predictability and their connection to precipitation. Finally, Section 4 concludes with a summary and remaining knowledge gaps.

## 2. Data and Methods

### 2.1. Model Forecast and Verification Data

In this study we evaluate the skill and predictability sources of seasonal AR frequency hindcasts and real-time forecasts from SPEAR, using the fifth generation European Centre for Medium Range Weather Forecasts reanalysis (ERA5, Hersbach et al., 2020) as a verification data set. SPEAR is a fully coupled prediction system, developed at the Geophysical Fluid Dynamics Laboratory, that includes the AM4 atmospheric model, LM4 land model, MOM6 ocean model, and SIS2 sea ice model (Delworth et al., 2020). In this study, SPEAR's native horizontal resolution in the atmosphere and land is about 50 km and ∼1° in the ocean, while ERA5's native resolution is 31 km. We analyze the data, for both SPEAR and ERA5, at a common 0.5° horizontal resolution.

SPEAR seasonal hindcasts, which cover the 1991–2020 period, are comprised of 15 ensemble members that are initialized on the first of the month and integrated forward for the next 12 months. The initialization incorporates

the SPEAR ocean data assimilation in combination with a separate set of ensemble coupled simulations with atmospheric conditions and sea surface temperatures (SSTs) nudged toward observations (see Lu et al. (2020) for additional details). The real-time SPEAR forecasts that have contributed to the NMME began in 2021 and follow the same initialization and integration procedures but incorporate 30 instead of 15 ensemble members; however, we include only the first 15 ensemble members for analysis consistency (note that we use the general term "forecasts" for the data set that combines the hindcasts with the real-time forecasts). We analyze all boreal winters (December-February, DJF), the season in which ARs are generally most active over the Northern Hemisphere (e.g., Mundhenk et al., 2016), from 1991 through 2023. The results are not sensitive to other reasonable definitions of winter (e.g., January-March).

We track ARs using daily mean data from both ERA5 and the SPEAR forecasts using the tracking method developed by Mundhenk et al. (2016), though we found similar results using the TempestExtreme tracking method (Ullrich & Zarzycki, 2017; see Figure S1 in Supporting Information S1). Previous studies have shown that AM4 faithfully captures many observed features of ARs (Dong et al., 2024; Zhao, 2020). Details on the AR tracking method, included in Supporting Information S1, are similar to those outlined in Tseng et al. (2021).

### 2.2. An Overview of Average Predictability Time Analysis

To determine the sources of AR predictability on seasonal timescales, we deploy average predictability time (APT) analysis (DelSole & Tippett, 2009a, 2009b), a method often used to identify predictable patterns in forecast data sets (e.g., Jia et al., 2015, 2022, 2023; Xiang et al., 2019; Yang et al., 2015). Although APT analysis relies on forecast uncertainty being well characterized by second-moment statistics, which may not hold over regions with low climatological AR frequency, these statistics remain valid over midlatitude regions with frequent AR occurrences. By analogy to empirical orthogonal function (EOF) analysis, which decomposes a data set into spatial patterns that optimize variance (e.g., DelSole & Tippett, 2022b; Wilks, 2011), APT analysis decomposes a data set into spatial patterns that optimize APT, defined as,

$$\mathrm{APT} = 2\sum_{\tau=0}^{\infty}\left(1-\frac{{\sigma_\tau}^2}{{\sigma_\infty}^2}\right)\Delta\tau \tag{1}$$

where ${\sigma_\infty}^2$ represents the climatological variance, ${\sigma_\tau}^2$ the forecast variance at lead time $\tau$, and $\Delta\tau$ the duration (i.e., number of days) separating each lead time. APT is a measure of the signal-to-noise ratio integrated over lead time that scales with the maximum lead in a forecast for which a signal can be detected above noise (see DelSole and Tippett (2009a, 2009b) for more details).

A first step in conducting APT analysis is defining the climatological and forecast covariance matrices, $\mathbf{\Sigma}_\infty$ and $\mathbf{\Sigma}_{\boldsymbol{\tau}}$. In this study, the climatological covariance matrix is defined as,

$$\mathbf{\Sigma}_\infty = \frac{\left(\boldsymbol{x}-\langle\boldsymbol{x}\rangle_{\tau,e}\right)\left(\boldsymbol{x}-\langle\boldsymbol{x}\rangle_{\tau,e}\right)^T}{(N-1)}, \tag{2}$$

where $\boldsymbol{x}$ is an $[M\times N]$ matrix containing $N = 4{,}950$ area-weighted AR frequency anomaly fields of $M = 29{,}120$ spatial grid points at a given verification time $t$ (target year, hereafter), lead time $\tau$ and ensemble member $e$ and where $\langle\cdot\rangle_*$ denotes an average over the dimension(s) indicated by the subscript(s). Thus, the target year $t$, lead time $\tau$ and ensemble member $e$ dimensions are aggregated into a single "state" dimension of length $N =$ (15 members $\times$ 10 lead times $\times$ 33 verification times) $= 4{,}950$. The forecast covariance matrix is defined for each lead time $\tau$ as,

$$\mathbf{\Sigma}_{\boldsymbol{\tau}} = \frac{\left\langle\left(\boldsymbol{x}_{t,\tau}-\langle\boldsymbol{x}_{t,\tau}\rangle_e\right)\left(\boldsymbol{x}_{t,\tau}-\langle\boldsymbol{x}_{t,\tau}\rangle_e\right)^T\right\rangle_t}{(N_{\mathrm{ens}}-1)}, \tag{3}$$

where $N_{\mathrm{ens}}$ is the length of the ensemble dimension (15 in this study) and $\boldsymbol{x}_{t,\tau}$ has dimensions $[M\times N_{\mathrm{ens}}]$. There are exactly 10 lead times for which $\mathbf{\Sigma}_{\boldsymbol{\tau}}$ is computed (denoted as lead 0 for 1 December initializations and lead 9 for 1 March initializations), meaning that APT is approximated as $\mathrm{APT}\approx 2\sum_{\tau=0}^{9\ \mathrm{months}}\left(1-\frac{{\sigma_\tau}^2}{{\sigma_\infty}^2}\right)\Delta\tau$, with an upper

bound of 18 months. For notational ease, we hereafter let $\boldsymbol{x}' \equiv \boldsymbol{x} - \langle \boldsymbol{x} \rangle_{\tau,e}$. (Also note that above, "anomaly" refers the deviation from the mean taken along the target year dimension only).

To identify the patterns that optimize APT, we solve the following generalized eigenvalue problem,

$$\boldsymbol{G}\boldsymbol{Q} = \boldsymbol{\lambda}\boldsymbol{\Sigma}_{\infty}\boldsymbol{Q}, \tag{4}$$

where $\boldsymbol{G} = 2\sum_{\tau=0}^{9}(\boldsymbol{\Sigma}_{\infty} - \boldsymbol{\Sigma}_{\tau})\Delta\tau$. The set of eigenvectors $\boldsymbol{Q} = \{\boldsymbol{q}_1, \boldsymbol{q}_2, \ldots, \boldsymbol{q}_M\}$ that satisfy 4 are termed *projection patterns* whose corresponding eigenvalues $\boldsymbol{\lambda} = \{\lambda_1, \lambda_2, \ldots, \lambda_M\}$ represent the APT of the *predictable variates*, $\boldsymbol{v} = \left\{\boldsymbol{q}_1{}^T\boldsymbol{x}', \boldsymbol{q}_2{}^T\boldsymbol{x}', \ldots, \boldsymbol{q}_M{}^T\boldsymbol{x}'\right\}$, where we have adopted the terminology used in DelSole and Tippett (2022a). The predictable variates quantify how these spatial patterns vary as a function of target year, lead time and ensemble member.

We define the $i$th *predictable pattern* by projecting $\boldsymbol{v}_i$ onto $\boldsymbol{x}'$, $\boldsymbol{p}_i = \frac{\boldsymbol{x}'\boldsymbol{v}_i^T}{(N-1)} = \boldsymbol{\Sigma}_{\infty}\boldsymbol{q}_i$, and we can decompose $\boldsymbol{x}'$ as follows,

$$\boldsymbol{x}' = \boldsymbol{p}_1\boldsymbol{v}_1 + \boldsymbol{p}_2\boldsymbol{v}_2 + \ldots + \boldsymbol{p}_M\boldsymbol{v}_M, \tag{5}$$

(DelSole & Tippett, 2009a, 2009b). Because the projection vectors obey the following constraint,

$$\boldsymbol{q}_i^T\boldsymbol{\Sigma}_{\infty}\boldsymbol{q}_j = \begin{cases} \mathbf{0} & \textit{if } i \neq j \\ \mathbf{1} & \textbf{otherwise} \end{cases} \tag{6}$$

the predictable variates are orthogonal along the state dimension. In other words, much like the principal components in EOF analysis are temporally uncorrelated, the predictable variates in APT analysis are also uncorrelated, but across three dimensions merged—lead time, verification time and ensemble member. Finally, as this analysis has been done such that the variance of each predictable variate is unity 6, the variance of the $i$th *predictable component*, $\boldsymbol{p}_i\boldsymbol{v}_i$, is entirely contained in the predictable pattern $\boldsymbol{p}_i$, such that the fraction of variance explained by the $i$th predictable component is given by $\boldsymbol{p}_i^T\,\boldsymbol{p}_i/\langle \boldsymbol{x}'^T\boldsymbol{x}' \rangle_{\tau,e}$.

Minimally, for 4 to have a unique solution, the size of the spatial dimension must be less than that of the state dimension, that is, $M < N$ (e.g., DelSole & Tippett, 2009b; Schneider & Griffies, 1999). To reduce the spatial dimensionality, we regularize by truncated EOF analysis (e.g., DelSole & Tippett, 2009b; Schneider & Griffies, 1999), by defining a truncated AR anomaly data set as $\boldsymbol{x}^* = \boldsymbol{E}\boldsymbol{x}$, where $\boldsymbol{E}$ is an $[M^* \times M]$ matrix containing $M^* = 25$ EOF patterns of $M$ spatial grid points, where $M^* < N$. The $M^* = 25$ EOFs explain approximately 78% of the total area-weighted variance (the results are not sensitive to the choice of $M^*$). After solving 4 in principal component space, we move the resulting patterns to physical space with $\boldsymbol{p} = \boldsymbol{E}\boldsymbol{p}^*$, where $\boldsymbol{p}^*$ represents the predictable patterns in principal component space. For more details on this, DelSole and Tippett (2022a) overview similar steps for predictable component analysis (e.g., DelSole & Chang, 2003; Schneider & Griffies, 1999). The Data Availability Statement includes an APT function written for Python.

## 3. Results

To begin, we show the first three predictable patterns in Figures 1a–1c resulting from the APT analysis of AR frequency, together with their associated precipitation patterns (Figures 1d–1f) expressed as a regression of SPEAR precipitation forecasts on the predictable variates (Figures 1g and 1h). Figure S2 in Supporting Information S1 depicts patterns 4 through 6, though we focus on patterns 1 through 3 because these patterns contain most of the predictability in the SPEAR AR frequency data set (Figure 2).

Spatially, patterns 1 and 3 are approximately out-of-phase (Figures 1a–1c) and characterized by three meridionally stacked anomalies of AR activity over the eastern North Pacific Ocean. Whereas pattern 1 features suppressed AR activity at about 45°N over the eastern North Pacific and flanked meridionally by enhanced AR activity, pattern 3 features enhanced AR activity at about 38°N and flanked meridionally by suppressed AR activity. Along the southeast U.S., where pattern 1 has a dipole oriented southeast to northwest and centered over

10.1029/2024GL112411

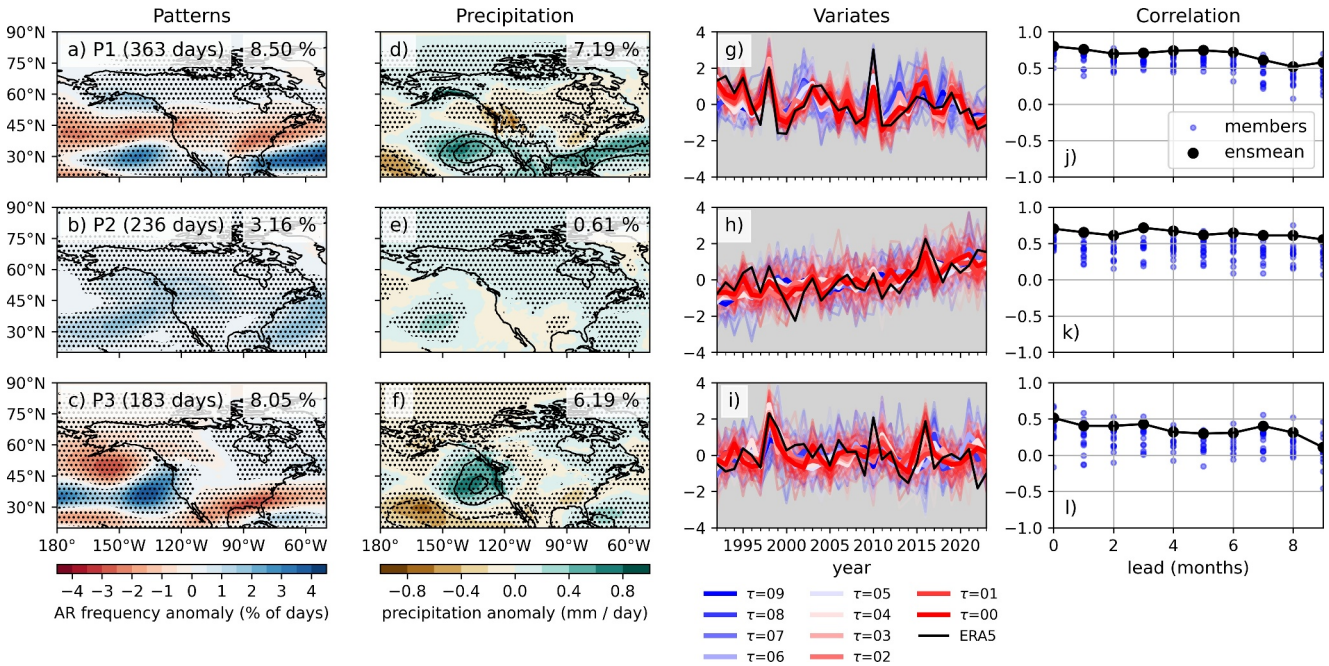


**Figure 1.** The (a–c) first three predictable patterns resulting from average predictability time (APT) Analysis, accompanied by the regression of panels (d–f) precipitation (shading) and extreme precipitation frequency (contours) onto the panels (g–i) predictable variates that vary as a function of target year (*x*-axis) and lead time in months (colors). The APT is indicated parenthetically in the 1st column and the explained variance (%) is also indicated in both the 1st and 2nd columns. The contour interval for the precipitation extremes is 1 day, and an extreme is defined as any day that exceeds the 90th percentile of all precipitating days. Thick lines in panels (g–i) show the ensemble mean while the thin translucent lines show the ensemble members, and the black line shows the ERA5 atmospheric river frequency anomalies projected onto the projection patterns (**Q**; see methods). The (j–l) correlations between ERA5 and the variates are shown as a function of lead time for both the ensemble mean (black) and each individual ensemble member (blue). Supporting Information S1 includes details about the regression and definition of precipitation extremes.

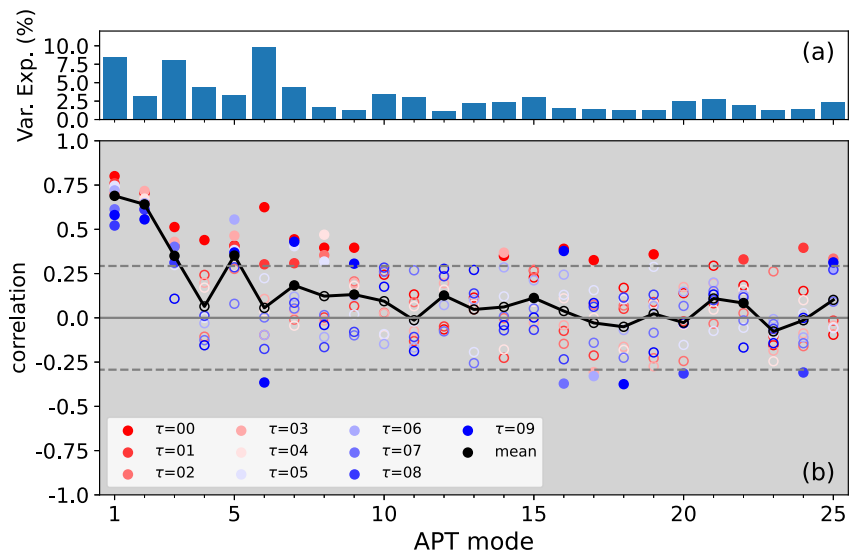


**Figure 2.** The (a) explained variance and (b) ensemble mean correlation skill as a function of lead time in months (colors) for each average predictability time (APT) mode (*x*-axis) resulting from APT analysis in the Pacific-North America domain (50°W–180°W and 20°N–90°N). The black line in panel (b) represents the correlation averaged over lead time. Statistical significance at the 10% level, based on a permutation test, is indicated with filled markers. The gray dashed lines also indicate the 5th and 95th percentiles from a Student's *t*-test with 30° of freedom. Supporting Information S1 includes additional details about the significance testing.

northern Florida, pattern 3 features a single negative anomaly. Overall pattern 3 is characterized by centers of action that collocate with the gradient in pattern 1 and vice-versa. This relationship differs from what is seen in pattern 2, which is more straightforwardly characterized by two centers of enhanced AR activity over the eastern Pacific Ocean and western Atlantic Ocean.

The seasonal mean (shading) and extreme (contours) precipitation changes that accompany the AR frequency anomalies share the same characteristics (Figures 1d–1f). The first pattern is associated with dry conditions over the U.S. Pacific Northwest that coincide with wet conditions over southern Alaska and over the U.S. Southwest, extending southeast through Mexico and into Florida (Figures 1d–1f). In contrast, pattern 3 is most strongly associated with wet conditions over the U.S. Pacific Northwest extending throughout most of California and coastal British Columbia, while pattern 2 primarily produces precipitation anomalies over the North Pacific Ocean.

By projecting ERA5 AR frequency anomalies onto the projection patterns, we see that ERA5 falls rather cleanly within the model spread (Figures 1g–1i) and the correlations evaluated for each mode (shown in Figures 1j–1l) decrease with increasing mode. The blue and black markers in Figures 1j–1l show that the ensemble mean consistently outperforms individual ensemble members, indicating how much the skill from a single realization may deviate from that of the ensemble mean. Modes 1 and 2 are skillfully predicted, with correlations for the ensemble mean SPEAR forecasts exceeding 0.5 for all leads up to 9 months and 0.7 for many leads (Figure 1j), while mode 3 has correlations of between 0.4 and 0.5 for most leads (Figures 1k and 1l). Also, Figures 1g–1i, which show the variates for each lead time and ensemble member (see legend), illustrate the key property that APT orders the modes by signal-to-noise ratio; the variates are clustered closer together in mode 1 than in mode 2 and in mode 2 more than in mode 3. Thus, the decrease in forecast skill from modes 1 to 3 follows the decrease in predictability.

In Figure 2, we show that although modes 1 through 3 account for much of the skill in SPEAR AR frequency forecasts, they account for only about 19% of the total seasonal AR frequency variance in the Pacific-North America domain (50°W–180°W and 20°N–90°N). Figure 2a shows the explained variance for each of the 25 APT modes, while Figure 2b shows the correlation with ERA5 for each lead time (colors) and the average correlation across all lead times (black). The only patterns which have unanimously positive skill over all leads are patterns 1 through 3 and 5, indicating, as stated earlier, that most of the AR frequency forecast skill is attributable to these four patterns. These results imply that seasonal AR prediction over the western U.S. is challenging. The forecast skill for the remaining patterns, in comparison, is not significant for most leads, despite mode 6 accounting for nearly 10% of the variance (Figures 2a and 2b).

In Figure S1 in Supporting Information S1, we examine mode 5, which is predicted with marginal skill (Figure 2b), and mode 6, which explains a large fraction of the AR frequency variance (Figure 2a). Mode 5 is associated with anomalous AR activity of the same sign along the western and eastern coasts of the U.S. and is associated with precipitation over the California coast (Figures S1b and S1e in Supporting Information S1). Despite evidence of modest skill, the predicted amplitude of mode 5 is generally much lower than that of verification (Figure S1h in Supporting Information S1). Mode 6 is characterized by large amplitude anomalies over the ocean, producing the large explained variance in this pattern (similar to the first EOF of AR activity shown in Tseng et al. (2021)). However, mode 6 has a weaker correlation with tropical variability (Figure S3 in Supporting Information S1), and is less predictable seasonally, than lower numbered APT modes.

Truncating the DJF AR frequency data set to the first three APT modes using 5, we find no appreciable difference between the skill of the resulting filtered data set and that of the original data set (Figures 3a–3c). We also tested this under cross validation to determine whether filtering forecast data can improve skill, as found in earlier studies (e.g., Jia et al., 2022). The results in Figures 3a–3c are obtained through a "leave-one-out" approach (e.g., Black et al., 2017)—reconstructing each year using slightly different APT patterns and variate values that are derived without including the data from the verification year in the APT analysis. Though this cross-validation approach unrealistically assumes knowledge of future data not available in a real-time forecast setting (Risbey et al., 2021), we find that filtering forecast data by APT patterns would not improve skill anyway (Figures 3c–3f). Thus, we limit our conclusion to these modes being the primary sources of skill over North America. Figure S3 in Supporting Information S1 shows the results without cross validation, and with the inclusion of only modes 1 and 3, indicating that the broad conclusions are insensitive to cross-validation and that the trend (mode 2) contributes only modestly to North American precipitation skill. Including mode 5 in the reconstruction does not significantly

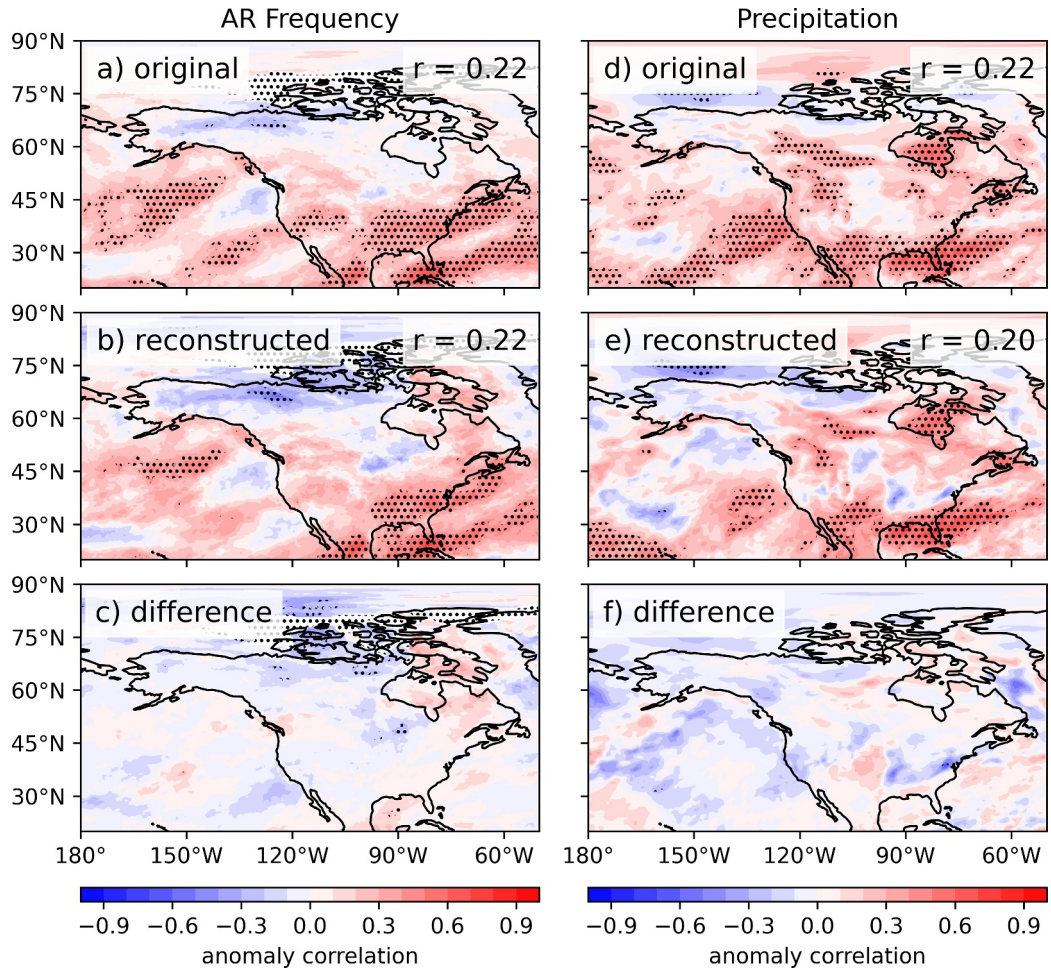


**Figure 3.** The correlation between ERA5 and SPEAR hindcasts averaged over lead time for (a, b) DJF atmospheric river frequency and (d, e) precipitation. Panels (b, e) show the correlation when the data set is truncated to three average predictability time modes, while panels (c, f) show the difference (as middle minus top). The overall correlation, defined by computing the covariance over both time and (area-weighted) space dimensions, is shown in the top right corner of panels (a, b, d, and e). Stippling indicates statistical significance based on a permutation test, where the false discovery rate is controlled using the Benjamini and Hochberg (1995) procedure at the $\alpha = 0.1$ level. Supporting Information S1 includes additional details about the significance testing.

improve the skill of the reconstructed data set, despite the variate for pattern 5 being relatively well forecast (Figure 2b). However, removing mode 3 from the reconstruction reduces skill slightly (not shown), implying that the skill of the DJF AR frequency is attributed nearly entirely to the first three modes.

Taking this reconstruction further, in Figures 3d–3f we reconstruct the precipitation data set from SPEAR forecasts using the regression patterns in Figures 1d–1f in place of the APT patterns in the reconstruction Equation 5. In Figures 3d–3f, this reconstructed precipitation data set has skill comparable to the original SPEAR precipitation hindcast (Figures 3d–3f). Also, note that applying APT analysis to precipitation directly instead of AR frequency results in nearly identical patterns to those shown in Figures 1d–1f (Figure S4 in Supporting Information S1).

That the first three APT modes explain nearly all seasonal mean AR frequency and precipitation prediction skill (Figure 3) prompts investigation into what physical processes drive these modes. By regressing precipitation (left), SST (right) and 500 hPa geopotential height (contours) on the predictable variates, we show in Figures 4a and 4d that mode 1 is associated with ENSO. In particular, the precipitation anomaly pattern and SST anomaly patterns in Figures 4a and 4d are canonical to ENSO (e.g., Philander, 1983), as supported by the correlation between the mode 1 variate and the Niño-3.4 index (along the aggregated state dimension in SPEAR) of 0.73.

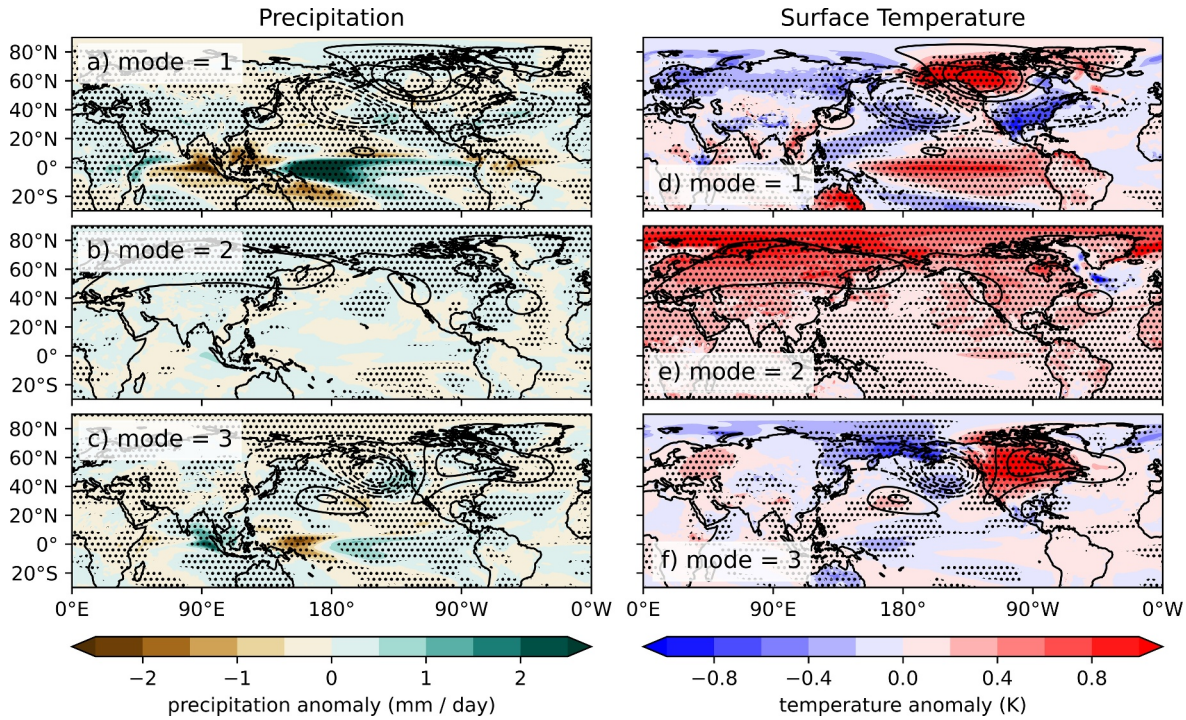


**Figure 4.** Regression of SPEAR (a–c) precipitation, (d–f) sea surface temperature and 500 hPa geopotential height (contours) on the predictable variates for average predictability time modes 1 through 3. The regression coefficient is computed along the entire merged "state" dimension (i.e., target year, lead time and ensemble member merged into a single dimension). The contour interval for geopotential height is 8 m where the zero contour is omitted. Stippling indicates statistical significance based on a permutation test, where the false discovery rate is controlled using the Benjamini and Hochberg (1995) procedure at the $\alpha = 0.1$ level. Supporting Information S1 includes additional details about the regression and significance testing.

That the first APT mode represents ENSO is also consistent with previous work showing skillful ENSO predictions in SPEAR for leads as long as 12 months (e.g., Lu et al., 2020).

Revisiting Figure 1g, we see the predictable variates for mode 1 peak during well-known El Niño years, including 1998 and 2010. Interestingly, while the predictable variates for mode 1 also peak in 2016, which was a strong El Niño winter, the projection of ERA5 data onto mode 1 does not peak in 2016 (Figure 1g). This aligns with 2016 winter season deviating substantially from the canonical ENSO signal (e.g., Kumar & Chen, 2020).

Turning our attention to mode 3, we see an interesting and perhaps unexpected result in Figures 2c and 2f: a wave train emanating from the tropics, as in mode 1, but in association with tropical precipitation and SST anomaly patterns distinct from that of canonical ENSO. Though this SST anomaly pattern resembles central and western pacific type ENSO events, the NCT and NWP indices (SST-based indices used to characterize central and western ENSO events; Ren & Jin, 2011), are correlated to the mode 3 variates in SPEAR with only modest values of 0.10 and −0.28, respectively. The zonal tripole of precipitation characterizing mode 3 extends from the western to central equatorial Pacific; precipitation is enhanced over the western warm pool and central equatorial Pacific, while suppressed between these regions, over the eastern flank of the western Pacific warm pool (hereafter, EWP; Figure 2c). Coinciding with the suppressed precipitation, the SST anomaly pattern is negative over the EWP, where an extratropical Rossby wave response appears to originate (Figure 2f; e.g., Hoskins & Karoly, 1981).

Consistent with the predictable patterns in Figures 1a and 1b, which were characterized by out-of-phase AR frequency anomalies, the geopotential height anomalies associated with modes 1 and 3 are also out of phase with each other. Both patterns 1 and 3 appear to represent a response to equatorial diabatic heating, given their great-circle-like trajectory in the geopotential height field that originates over the subtropical North Pacific (e.g., Hoskins & Karoly, 1981). Considering their tropical origin, it is possible that patterns 1 and 3 owe their out-of-phase extratropical anomalies to a zonal displacement of the equatorial diabatic heating anomalies driving them, as evidenced by the precipitation and SST anomaly fields in Figures 4a, 4c, 4d, and 4f. Specifically, comparing

Figures 4d and 4f, the positive SST anomaly for mode 1 maximizes east of 180°, whereas the negative SST anomaly for pattern 3 maximizes west of 180°.

In contrast with modes 1 and 3, mode 2 (as well as modes 4–6; Figure S2 in Supporting Information S1) does not exhibit a clear teleconnection with the tropics. Instead, the second APT mode of seasonal AR variability is dominated by the trend. The predictable variate for this pattern clearly trends positively (Figure 1i) and when regressing the SST onto the predictable variate, we see the global warming signal (Figure 4e), including Arctic amplification (e.g., Previdi et al., 2021) and the North Atlantic warming hole (e.g., Keil et al., 2020). The uniformly positive AR anomalies in mode 2 (Figure 1b) also agree with projected AR changes reviewed by Payne et al. (2020).

The emergence of the trend in the second mode raises the following question: why does ENSO have a larger APT than the trend? Presumably the trend would be the first APT mode if more than 9 months of lead time were included in the forecast, as the signal-to-noise ratio for ENSO would decline with lead while remaining relatively constant with lead for the trend. Another interesting question is whether SPEAR correctly represents the relationship between these predictable modes and the SST-driven teleconnections. When regressing ERA5 data on its predictable variates, the 500 hPa geopotential height resembles that from SPEAR for both mode 1 and mode 3 (cf. Figure 4c and Figure S5c in Supporting Information S1), however ERA5's SST anomaly pattern for mode 3 includes not only a negative anomaly over the EWP, but also a considerable El Niño anomaly, albeit with limited zonal extent (Figure S6–S8 in Supporting Information S1). This mode 3 El Niño bias is reduced for shorter lead times (Figure S8 in Supporting Information S1). Further investigation of this bias is deferred to future work.

## 4. Summary and Conclusions

In this study, we applied APT analysis to determine the dominant patterns and sources of DJF AR predictability over North America in SPEAR hindcast and forecast simulations over 9-month of lead time. The first three components of APT analysis together explain nearly all of the seasonal AR frequency skill and account for about 19% of the total DJF variance in the Pacific-North America domain. The first mode represents the AR response to ENSO, while the third mode is out of phase with the first and reflects a response to tropical variability in the EWP. In contrast with modes 1 and 3, the second APT mode is unrelated to tropical variability and instead is closely related to the trend due to anthropogenic forcing. Modes 1 and 3 feature seasonal AR frequency and precipitation anomalies over North America.

Previous work suggests that canonical ENSO-based precipitation forecasts over North America are difficult to outperform (Jiang et al., 2022), prompting the question, "is there any source of seasonal precipitation predictability beyond ENSO?" That the second and third APT modes contribute to skillful AR frequency and precipitation forecasts implies sources of predictability beyond canonical ENSO do indeed exist, for both ARs and precipitation. Specifically, tropical variability over the EWP in mode 3 drives significant extratropical circulation anomalies that are out of phase with the canonical ENSO circulation response and can aid in AR prediction. Furthermore, mode 2 implies that anthropogenic forcing increases the frequency of ARs from one year to the next, though these increases in AR frequency are unaccompanied by pronounced seasonal mean precipitation anomalies over North America.

Given that the interest in seasonal AR prediction is rooted in how the accompanying precipitation impacts society, another question of interest is whether precipitation predictability is tied to AR predictability generally. We found that nearly all of the skill in SPEAR's seasonal mean precipitation forecasts can be reconstructed with the first three APT modes of seasonal AR frequency, and conclude that the predictable precipitation signal is nearly entirely associated with that of AR frequency. In other words, seasonal DJF AR and precipitation predictability over North America are driven by the same sources.

One of the more unexpected findings in this study was mode 3 featuring a pattern that does not match obviously with any previously identified teleconnection. It is possible that mode 3 represents ENSO diversity in some way (e.g., Ashok et al., 2007). The fact that mode 3 correlates to ENSO in ERA5, but not in SPEAR, supports this possibility while also raising the possibility that the model does not capture a real-world mode 3-ENSO relationship. However, more research is needed to rule out the possibility that mode 3 is itself an independent phenomenon. Future work should also investigate the extent to which the results presented in this study depend on the specific model used.

## Data Availability Statement

The SPEAR data supporting this study is provided by Clark et al. (2024). Example APT scripts are also provided by Clark et al. (2024). ERA5 data used in this study is provided by Hersbach et al. (2017).

**Acknowledgments**
We thank Xiaosong Yang and Wenhao Dong for reviewing an earlier version of this manuscript and providing insightful comments. We also thank Tim DelSole for helpful correspondence regarding APT analysis. This study was supported by Award NA22OAR4050663D from the National Oceanic and Atmospheric Administration, U.S. Department of Commerce. Joseph P. Clark also acknowledges support from the Cooperative Institute for Modeling the Earth System under Award NA18OAR4320123 from the National Oceanic and Atmospheric Administration, U.S. Department of Commerce. The statements, findings, conclusions, and recommendations are those of the authors and do not necessarily reflect the views of the National Oceanic and Atmospheric Administration, or the U.S. Department of Commerce.

## References

Ashok, K., Behera, S. K., Rao, S. A., Weng, H., & Yamagata, T. (2007). El Niño Modoki and its possible teleconnection. *Journal of Geophysical Research*, *112*(C11), C11007. https://doi.org/10.1029/2006jc003798

Baggett, C. F., Barnes, E. A., Maloney, E. D., & Mundhenk, B. D. (2017). Advancing atmospheric river forecasts into subseasonal-to-seasonal time scales. *Geophysical Research Letters*, *44*(14), 7528–7536. https://doi.org/10.1002/2017gl074434

Benjamini, Y., & Hochberg, Y. (1995). Controlling the false discovery rate: A practical and powerful approach to multiple testing. *Journal of the Royal Statistical Society: Series B*, *57*(1), 289–300. https://doi.org/10.1111/j.2517-6161.1995.tb02031.x

Black, J., Johnson, N. C., Baxter, S., Feldstein, S. B., Harnos, D. S., & L'Heureux, M. L. (2017). The predictors and forecast skill of Northern Hemisphere teleconnection patterns for lead times of 3–4 weeks. *Monthly Weather Review*, *145*(7), 2855–2877. https://doi.org/10.1175/mwr-d-16-0394.1

Clark, J. P., Johnson, N. C., Park, M., Bernardez, M., & Delworth, T. (2024). Dataset supporting "predictable patterns of seasonal atmospheric river variability over North America during winter" [Dataset]. *Zenodo*. https://doi.org/10.5281/zenodo.13647589

Corringham, T. W., Ralph, F. M., Gershunov, A., Cayan, D. R., & Talbot, C. A. (2019). Atmospheric rivers drive flood damages in the western United States. *Science Advances*, *5*(12), eaax4631. https://doi.org/10.1126/sciadv.aax4631

DeFlorio, M. J., Sengupta, A., Castellano, C. M., Wang, J., Zhang, Z., Gershunov, A., et al. (2024). From California's extreme drought to major flooding: Evaluating and synthesizing experimental seasonal and subseasonal forecasts of landfalling atmospheric rivers and extreme precipitation during winter 2022/23. *Bulletin of the American Meteorological Society*, *105*(1), E84–E104. https://doi.org/10.1175/bams-d-22-0208.1

DeFlorio, M. J., Waliser, D. E., Guan, B., Lavers, D. A., Ralph, F. M., & Vitart, F. (2018). Global assessment of atmospheric river prediction skill. *Journal of Hydrometeorology*, *19*(2), 409–426. https://doi.org/10.1175/jhm-d-17-0135.1

DeFlorio, M. J., Waliser, D. E., Guan, B., Ralph, F. M., & Vitart, F. (2019). Global evaluation of atmospheric river subseasonal prediction skill. *Climate Dynamics*, *52*(5–6), 3039–3060. https://doi.org/10.1007/s00382-018-4309-x

DeFlorio, M. J., Waliser, D. E., Ralph, F. M., Guan, B., Goodman, A., Gibson, P. B., et al. (2019). Experimental subseasonal-to-seasonal (S2S) forecasting of atmospheric rivers over the western United States. *Journal of Geophysical Research: Atmospheres*, *124*(21), 11242–11265. https://doi.org/10.1029/2019jd031200

DelSole, T., & Chang, P. (2003). Predictable component analysis, canonical correlation analysis, and autoregressive models. *Journal of the Atmospheric Sciences*, *60*(2), 409–416. https://doi.org/10.1175/1520-0469(2003)060<0409:pcacca>2.0.co;2

DelSole, T., & Tippett, M. (2022a). Predictable component analysis. In *Statistical methods for climate scientists* (pp. 418–445). Cambridge University Press. https://doi.org/10.1017/9781108659055.019

DelSole, T., & Tippett, M. (2022b). Principal component analysis. In *Statistical methods for climate scientists* (pp. 273–297). Cambridge University Press. https://doi.org/10.1017/9781108659055.013

DelSole, T., & Tippett, M. K. (2009a). Average predictability time. Part I: Theory. *Journal of the Atmospheric Sciences*, *66*(5), 1172–1187. https://doi.org/10.1175/2008jas2868.1

DelSole, T., & Tippett, M. K. (2009b). Average predictability time. Part II: Seamless diagnoses of predictability on multiple time scales. *Journal of the Atmospheric Sciences*, *66*(5), 1188–1204. https://doi.org/10.1175/2008jas2869.1

Delworth, T. L., Cooke, W. F., Adcroft, A., Bushuk, M., Chen, J. H., Dunne, K. A., et al. (2020). SPEAR: The next generation GFDL modeling system for seasonal to multidecadal prediction and projection. *Journal of Advances in Modeling Earth Systems*, *12*(3), e2019MS001895. https://doi.org/10.1029/2019ms001895

Dettinger, M. (2011). Climate change, atmospheric rivers, and floods in California–a multimodel analysis of storm frequency and magnitude changes. *Journal of the American Water Resources Association*, *47*(3), 514–523. https://doi.org/10.1111/j.1752-1688.2011.00546.x

Dettinger, M. D. (2013). Atmospheric rivers as drought busters on the US West Coast. *Journal of Hydrometeorology*, *14*(6), 1721–1732. https://doi.org/10.1175/jhm-d-13-02.1

Dettinger, M. D., Ralph, F. M., Das, T., Neiman, P. J., & Cayan, D. R. (2011). Atmospheric rivers, floods and the water resources of California. *Water*, *3*(2), 445–478. https://doi.org/10.3390/w3020445

Dettinger, M. D., Ralph, F. M., & Lavers, D. A. (2015). Setting the stage for a global science of atmospheric rivers. *EOS, Earth and Space Science News*, *96*, 38675. https://doi.org/10.1029/2015eo038675

Ding, Q., & Wang, H. (2024). Influences of large scale circulation and atmospheric rivers on US winter precipitation beyond ENSO. *Journal of Climate*, *37*(17), 4577–4593. https://doi.org/10.1175/jcli-d-23-0723.1

Dong, W., Zhao, M., Tan, Z., & Ramaswamy, V. (2024). Atmospheric rivers over eastern US affected by Pacific/North America pattern. *Science Advances*, *10*(4), eadj3325. https://doi.org/10.1126/sciadv.adj3325

Guan, B., Molotch, N. P., Waliser, D. E., Fetzer, E. J., & Neiman, P. J. (2010). Extreme snowfall events linked to atmospheric rivers and surface air temperature via satellite measurements. *Geophysical Research Letters*, *37*(20), L20401. https://doi.org/10.1029/2010gl044696

Hersbach, H., Bell, B., Berrisford, P., Hirahara, S., Horányi, A., Muñoz-Sabater, J., et al. (2017). Complete ERA5 from 1940: Fifth generation of ECMWF atmospheric reanalyses of the global climate [Dataset]. *Copernicus Climate Change Service (C3S) Data Store (CDS)*. https://doi.org/10.24381/cds.143582cf

Hersbach, H., Bell, B., Berrisford, P., Hirahara, S., Horányi, A., Muñoz-Sabater, J., et al. (2020). The ERA5 global reanalysis. *The Quarterly Journal of the Royal Meteorological Society*, *146*(730), 1999–2049. https://doi.org/10.1002/qj.3803

Hoskins, B. J., & Karoly, D. J. (1981). The steady linear response of a spherical atmosphere to thermal and orographic forcing. *Journal of the Atmospheric Sciences*, *38*(6), 1179–1196. https://doi.org/10.1175/1520-0469(1981)038<1179:tslroa>2.0.co;2

Jia, L., Delworth, T. L., Kapnick, S., Yang, X., Johnson, N. C., Cooke, W., et al. (2022). Skillful seasonal prediction of North American summertime heat extremes. *Journal of Climate*, *35*(13), 4331–4345. https://doi.org/10.1175/jcli-d-21-0364.1

Jia, L., Delworth, T. L., Yang, X., Cooke, W., Johnson, N. C., McHugh, C., & Lu, F. (2023). Seasonal prediction of North American wintertime cold extremes in the GFDL SPEAR forecast system. *Climate Dynamics*, *61*(3), 1769–1781. https://doi.org/10.1007/s00382-022-06655-w

Jia, L., Yang, X., Vecchi, G. A., Gudgel, R. G., Delworth, T. L., Rosati, A., et al. (2015). Improved seasonal prediction of temperature and precipitation over land in a high-resolution GFDL climate model. *Journal of Climate*, *28*(5), 2044–2062. https://doi.org/10.1175/jcli-d-14-00112.1

Jiang, X., Waliser, D. E., Gibson, P. B., Chen, G., & Guan, W. (2022). Why seasonal prediction of California winter precipitation is challenging. *Bulletin of the American Meteorological Society*, *103*(12), E2688–E2700. https://doi.org/10.1175/bams-d-21-0252.1

Keil, P., Mauritsen, T., Jungclaus, J., Hedemann, C., Olonscheck, D., & Ghosh, R. (2020). Multiple drivers of the North Atlantic warming hole. *Nature Climate Change*, *10*(7), 667–671. https://doi.org/10.1038/s41558-020-0819-8

Kirtman, B. P., Min, D., Infanti, J. M., Kinter, J. L., Paolino, D. A., Zhang, Q., et al. (2014). The North American multimodel ensemble: Phase-1 seasonal-to-interannual prediction; phase-2 toward developing intraseasonal prediction. *Bulletin of the American Meteorological Society*, *95*(4), 585–601. https://doi.org/10.1175/bams-d-12-00050.1

Kumar, A., & Chen, M. (2020). Understanding skill of seasonal mean precipitation prediction over California during boreal winter and role of predictability limits. *Journal of Climate*, *33*(14), 6141–6163. https://doi.org/10.1175/jcli-d-19-0275.1

Lu, F., Harrison, M. J., Rosati, A., Delworth, T. L., Yang, X., Cooke, W. F., et al. (2020). GFDL's SPEAR seasonal prediction system: Initialization and ocean tendency adjustment (OTA) for coupled model predictions. *Journal of Advances in Modeling Earth Systems*, *12*(12), e2020MS002149. https://doi.org/10.1029/2020ms002149

Mundhenk, B. D., Barnes, E. A., & Maloney, E. D. (2016). All-season climatology and variability of atmospheric river frequencies over the North Pacific. *Journal of Climate*, *29*(13), 4885–4903. https://doi.org/10.1175/jcli-d-15-0655.1

Mundhenk, B. D., Barnes, E. A., Maloney, E. D., & Baggett, C. F. (2018). Skillful empirical subseasonal prediction of landfalling atmospheric river activity using the Madden–Julian Oscillation and quasi-biennial oscillation. *npj Climate and Atmospheric Science*, *1*(1), 20177. https://doi.org/10.1038/s41612-017-0008-2

Nardi, K. M., Barnes, E. A., & Ralph, F. M. (2018). Assessment of numerical weather prediction model reforecasts of the occurrence, intensity, and location of atmospheric rivers along the West Coast of North America. *Monthly Weather Review*, *146*(10), 3343–3362. https://doi.org/10.1175/mwr-d-18-0060.1

Payne, A. E., Demory, M. E., Leung, L. R., Ramos, A. M., Shields, C. A., Rutz, J. J., et al. (2020). Responses and impacts of atmospheric rivers to climate change. *Nature Reviews Earth and Environment*, *1*(3), 143–157. https://doi.org/10.1038/s43017-020-0030-5

Philander, S. G. H. (1983). El Nino Southern Oscillation phenomena. *Nature*, *302*(5906), 295–301. https://doi.org/10.1038/302295a0

Previdi, M., Smith, K. L., & Polvani, L. M. (2021). Arctic amplification of climate change: A review of underlying mechanisms. *Environmental Research Letters*, *16*(9), 093003. https://doi.org/10.1088/1748-9326/ac1c29

Ralph, F. M., Neiman, P. J., Wick, G. A., Gutman, S. I., Dettinger, M. D., Cayan, D. R., & White, A. B. (2006). Flooding on California's Russian River: Role of atmospheric rivers. *Geophysical Research Letters*, *33*(13), L13801. https://doi.org/10.1029/2006gl026689

Ren, H. L., & Jin, F. F. (2011). Niño indices for two types of ENSO. *Geophysical Research Letters*, *38*(4), L04704. https://doi.org/10.1029/2010gl046031

Risbey, J. S., Squire, D. T., Black, A. S., DelSole, T., Lepore, C., Matear, R. J., et al. (2021). Standard assessments of climate forecast skill can be misleading. *Nature Communications*, *12*(1), 4346. https://doi.org/10.1038/s41467-021-23771-z

Schneider, T., & Griffies, S. M. (1999). A conceptual framework for predictability studies. *Journal of Climate*, *12*(10), 3133–3155. https://doi.org/10.1175/1520-0442(1999)012<3133:acffps>2.0.co;2

Tseng, K. C., Johnson, N. C., Kapnick, S. B., Delworth, T. L., Lu, F., Cooke, W., et al. (2021). Are multiseasonal forecasts of atmospheric rivers possible? *Geophysical Research Letters*, *48*(17), e2021GL094000. https://doi.org/10.1029/2021gl094000

Ullrich, P. A., & Zarzycki, C. M. (2017). TempestExtremes: A framework for scale-insensitive pointwise feature tracking on unstructured grids. *Geoscientific Model Development*, *10*(3), 1069–1090. https://doi.org/10.5194/gmd-10-1069-2017

Wick, G. A., Neiman, P. J., Ralph, F. M., & Hamill, T. M. (2013). Evaluation of forecasts of the water vapor signature of atmospheric rivers in operational numerical weather prediction models. *Weather and Forecasting*, *28*(6), 1337–1352. https://doi.org/10.1175/waf-d-13-00025.1

Wilks, D. S. (2011). Principal component (EOF) analysis. In R. Dmowska, D. Hartmann, & H. T. Rossby (Eds.). *International geophysics*, (Edn. 3, Vol. 100, pp. 519–562). Academic Press. https://doi.org/10.1016/b978-0-12-385022-5.00012-9

Xiang, B., Lin, S. J., Zhao, M., Johnson, N. C., Yang, X., & Jiang, X. (2019). Subseasonal week 3–5 surface air temperature prediction during boreal wintertime in a GFDL model. *Geophysical Research Letters*, *46*(1), 416–425. https://doi.org/10.1029/2018gl081314

Yang, X., Vecchi, G. A., Gudgel, R. G., Delworth, T. L., Zhang, S., Rosati, A., et al. (2015). Seasonal predictability of extratropical storm tracks in GFDL's high-resolution climate prediction model. *Journal of Climate*, *28*(9), 3592–3611. https://doi.org/10.1175/jcli-d-14-00517.1

Zhang, W., Xiang, B., Tseng, K. C., Johnson, N. C., Harris, L., Delworth, T., & Kirtman, B. (2024). Subseasonal-to-seasonal (S2S) prediction of atmospheric rivers in the Northern Winter. *npj Climate and Atmospheric Science*, *7*(1), 275. https://doi.org/10.1038/s41612-024-00827-7

Zhang, Z., Ralph, F. M., & Zheng, M. (2019). The relationship between extratropical cyclone strength and atmospheric river intensity and position. *Geophysical Research Letters*, *46*(3), 1814–1823. https://doi.org/10.1029/2018gl079071

Zhao, M. (2020). Simulations of atmospheric rivers, their variability, and response to global warming using GFDL's new high-resolution general circulation model. *Journal of Climate*, *33*(23), 10287–10303. https://doi.org/10.1175/jcli-d-20-0241.1

Zhou, Y., & Kim, H. M. (2018). Prediction of atmospheric rivers over the North Pacific and its connection to ENSO in the North American multimodel ensemble (NMME). *Climate Dynamics*, *51*(5), 1623–1637. https://doi.org/10.1007/s00382-017-3973-6

Zhu, Y., & Newell, R. E. (1998). A proposed algorithm for moisture fluxes from atmospheric rivers. *Monthly Weather Review*, *126*(3), 725–735. https://doi.org/10.1175/1520-0493(1998)126<0725:apafmf>2.0.co;2

## References From the Supporting Information

Wilks, D. S. (2006). On "field significance" and the false discovery rate. *Journal of Applied Meteorology and Climatology*, *45*(9), 1181–1189. https://doi.org/10.1175/jam2404.1

Wilks, D. S. (2011). Frequentist statistical inference. In R. Dmowska, D. Hartmann, & H. T. Rossby (Eds.). *International geophysics*, (Edn. 3, Vol. 100, pp. 133–186). Academic Press. https://doi.org/10.1016/b978-0-12-385022-5.00005-1